energies

MDPI

Article

The Influence of Fe on the Structure and Hydrogen Sorption Properties of Ti—V-Based Metal Hydrides

Magnus M. Nygård [1,2], Magnus H. Sørby [1,*], Arne A. Grimenes [2] and Bjørn C. Hauback [1]

[1] Department for Neutron Materials Characterization, Institute for Energy Technology, P.O. Box 40, NO-2027 Kjeller, Norway; magnus.moe.nygaard@ife.no (M.M.N.); bjorn.hauback@ife.no (B.C.H.)
[2] Department of Mathematical Sciences and Technology, Norwegian University of Life Sciences, Universitetstunet 3, NO-1433 Ås, Norway; arne.grimenes@nmbu.no
* Correspondence: magnus.sorby@ife.no

Received: 22 April 2020; Accepted: 29 May 2020; Published: 4 June 2020



Abstract: Ti—V-based metal hydrides have decent overall performance as hydrogen storage materials, but V is expensive and it is therefore tempting to replace it by less expensive ferrovanadium containing about 20% Fe. In the present work we have investigated how Fe influences the structure and hydrogen storage properties of $(Ti_{0.7}V_{0.3})_{1-z}Fe_z$ alloys with $z \in \{0, 0.03, 0.06, 0.1, 0.2, 0.3\}$ using synchrotron radiation powder X-ray diffraction, thermogravimetric analysis, differential scanning calorimetry and manometric measurements performed in a Sieverts apparatus. The alloys form body-centered cubic (bcc) crystal structures for all considered values of z, and the addition of Fe causes the unit cell to contract. When exposed to hydrogen gas, the bcc alloys form face-centered cubic (fcc) hydrides if $z \leq 0.1$ while other hydrogen-containing phases are formed for higher Fe-contents. The hydrogen capacities of the fcc hydrides at 20 bar are not significantly influenced by the addition of Fe and reach 3.2(3) wt% in $(Ti_{0.7}V_{0.3})_{0.9}Fe_{0.1}H_{1.6(2)}$. For higher Fe contents the hydrogen capacity is decreased. The absorption kinetics are fast and the reactions are complete within minutes when the alloys are exposed to 20 bar H_2 at room temperature. Increasing Fe content reduces the desorption enthalpy, onset temperature and activation energy.

Keywords: metal hydrides; hydrogen storage; in situ synchrotron radiation powder X-ray diffraction; activation energy for hydrogen desorption

1. Introduction

Hydrogen is considered a promising energy carrier for the future as it possesses the highest gravimetric energy density of any known substance. Moreover, it can be produced by environmentally friendly methods, such as water electrolysis, and is therefore considered an attractive energy vector for the future. However, hydrogen assumes a diatomic gas phase with very low density at ambient conditions. This makes compact and safe storage a technological challenge. In this regard, storage in metal hydrides is an interesting solution as such systems achieve very high volumetric hydrogen densities in the range 100–150 kg H_2/m^3 at ambient conditions [1,2]. Some metal hydrides also have relatively high gravimetric hydrogen densities, e.g., 18.4 wt% H in $LiBH_4$ and 7.6 wt% H in MgH_2. However, applications are often prevented by unfavourable kinetics, thermodynamics and/or non-reversibility [3,4]. Non-reversibility is usually not an issue for interstitial hydrides, but the gravimetric hydrogen densities in these materials are quite modest, e.g., 1.37 wt.% H in $LaNi_5H_6$. Nevertheless, interstitial hydrides are attractive for stationary applications where the weight of the hydrogen-storage unit can be compromised for higher volumetric hydrogen densities.

Body-centered cubic (bcc) solid solutions based on Ti and V is one class of interstitial hydrides with potential for hydrogen storage applications. These materials form face-centered cubic (fcc)

hydrides and achieve decent gravimetric hydrogen densities around 4 wt%. Their drawbacks includes slow kinetics and surface passivation [5–10]. Nevertheless, it has been shown that the surface can be activated if small amounts of a third metal with radius at least 5% smaller than that of V, e.g., Fe, is added to the Ti−V-system [11,12]. This is interesting from an economical perspective as it opens for the substitution of expensive, high purity V by much cheaper ferrovanadium containing about 20% Fe. In this context it is of fundamental interest to determine how the introduction of Fe influences the crystal structure and hydrogen sorption properties of Ti−V-based metal hydrides.

The V-rich part of such Ti−V−Fe metal hydride systems has been studied in the literature [13,14]. Lynch et al. have reported that increasing amounts of Fe decrease both the enthalpy and entropy of desorption while increasing amounts of Ti has the opposite effect [13]. A similar observation was made by Kagawa et al. who found that the hydrogen absorption rate increased markedly with Ti content while it decreased by the addition of Fe to the system [14]. The kinetic and thermodynamic properties of the alloy can therefore be tuned to specific applications.

For the Ti-rich part of the system it was recently demonstrated by neutron total scattering and transmission electron microscopy (TEM) that Fe form clusters in $(Ti_{0.7}V_{0.3})_{0.9}Fe_{0.1}D_{1.7}$ [15]. Thus, the maximum hydrogen storage capacity is reduced due to the fact that Fe does not form stable hydrides at ambient conditions. In this work we consider how the structure and hydrogen sorption properties of $(Ti_{0.7}V_{0.3})_{1-z}Fe_z$ change as a function of the Fe content in the solid solution. It should be noted that replacing V by ferrovanadium in $Ti_{0.7}V_{0.3}$ corresponds to choosing $z \approx 0.07$.

2. Results and Discussion

2.1. Ex Situ SR-PXD Structural Analysis

Figure 1 shows Rietveld refinements of a representative selection of synchrotron radiation powder X-ray diffraction (SR-PXD) patterns for the hydrides and the corresponding alloys after desorption. Refinements of the other systems are shown in Figure S1 in the Supplementary Information. The main phase of the alloys are bcc ($Im\bar{3}m$) if $z \leq 0.2$. Tables 1 and 2 presents lattice parameters obtained from the Rietveld refinements of the alloys and hydrides, respectively. It can be seen that the bcc unit cell parameter decreases as the amount of Fe in the alloy increases. A hexagonal close-packed phase (hcp, $P6_3/mmc$) is present for all samples with $z \leq 0.1$. Table 1 shows that the hcp lattice parameters are comparable to those for α-Ti ($a = 2.95111(6)$ Å, $c = 4.68433(10)$ Å [16]). A C14 Laves phase ($P6_3/mmc$) is present for $z = 0.3$, and the oxide Ti_4Fe_2O ($Fd\bar{3}m$) is observed in the three most Fe-rich alloys. Figure 2 shows the weight fractions of the different phases as a function of Fe-content. The hcp phase is an impurity for which the amount decreases with increasing Fe-content. The C14 Laves phase is the main phase of the most Fe-rich composition. It can also be seen that the amount of oxide increases linearly from $z = 0.1$ to $z = 0.3$.

For the fcc hydrides, the (111) peaks ($2\theta \approx 16°$) are slightly shifted towards higher scattering angles when compared to the expected peak positions. The (200) peaks ($2\theta \approx 18°$) are shifted in the opposite direction. This is reflected by subtle features in the difference curves in Figure 1, and the lattice parameters a_{fcc} in Table 2 are thus more uncertain than the standard deviations calculated by the Rietveld code. Deviations like the one outlined above might indicate stacking faults in fcc structures [17]. Moreover, it has been discussed by Balogh et al. [18] that such planar defects might cause the diffraction peaks to assume asymmetric and broadened profiles. Similar observations were also found in a TEM study of $Ti_{0.7}V_{0.3}$ [19]. Hence, planar defects seems to explain the slight misfits encountered during the structural refinements of the hydrides. It should be noted that the deviations from undistorted fcc profiles increase with the amount of Fe in the systems. The minuscule Bragg peaks from Ti_4Fe_2O in the SR-PXD data for the alloy with $z = 0.1$, are not observed in the corresponding hydride sample. This is probably due to overlap with peaks from the fcc hydride. The oxide phase was, therefore, not included in the Rietveld refinement of this hydride. Furthermore, the fcc hydride is unable to form for the two most Fe-rich systems, $z = 0.2$ and $z = 0.3$, under the

current experimental conditions. This might be related to the electron-configuration of the system as illustrated by the valence electron concentration *VEC* of the alloys (see Table 2). Single-phase fcc hydrides are obtained when $VEC < 5.04$. This is in agreement with Lynch et al. who proposed $VEC = 5.1$ as a limiting value for formation of fcc hydrides [13].

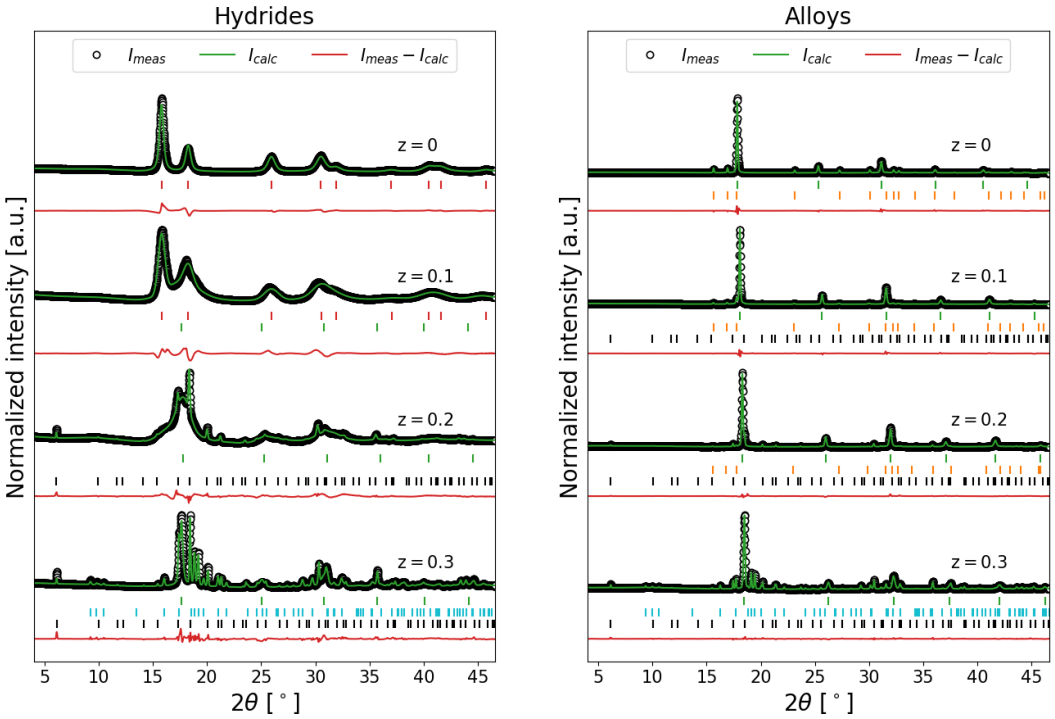

Figure 1. Rietveld refinements of the SR-PXD patterns for $(Ti_{0.7}V_{0.3})_{1-z}Fe_zH_x$ and the corresponding alloys after desorption. Green ticks indicates a bcc phase ($Im\bar{3}m$), red ticks indicates a fcc phase ($Fm\bar{3}m$), orange ticks indicates an hcp phase ($P6_3/mmc$), cyan ticks indicates a C14 Laves phase ($P6_3/mmc$) and black ticks indicates Ti_4Fe_2O ($Fd\bar{3}m$). $\lambda = 0.6973$ Å.

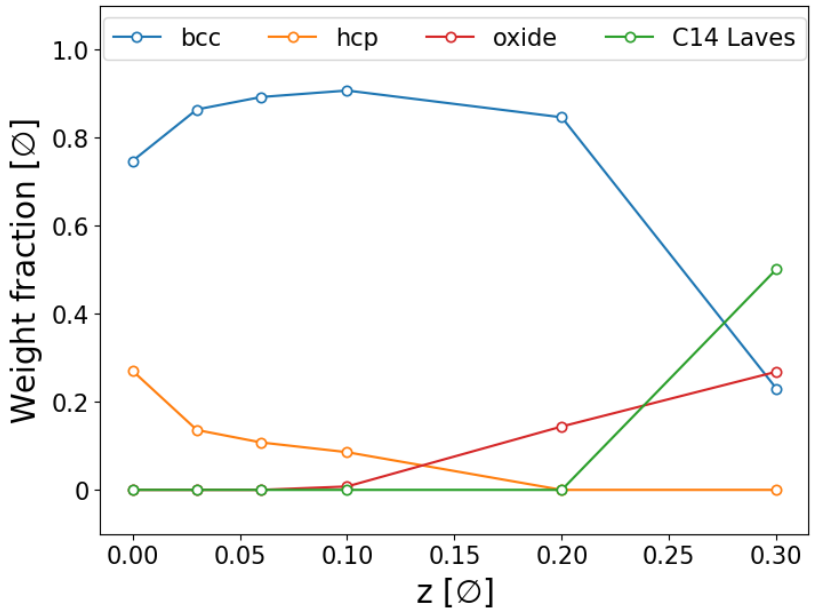

Figure 2. The weight fractions of the different phases present in $(Ti_{0.7}V_{0.3})_{1-z}Fe_z$ obtained from the Rietveld refinements. The error bars are within the data points.

Table 1. The lattice parameters obtained from the Rietveld refinements of the synchrotron radiation powder X-ray diffraction (SR-PXD) patterns for $(Ti_{0.7}V_{0.3})_{1-z}Fe_z$. The valence-electron concentrations *VEC* of the nominal compositions are also shown.

z	*VEC* [∅]	a_{bcc} [Å]	a_{hcp} [Å]	c_{hcp} [Å]	a_{Laves} [Å]	c_{Laves} [Å]
0	4.30	3.18291(11)	2.95913(12)	4.7365(2)	-	-
0.03	4.41	3.17578(11)	2.95945(15)	4.7385(3)	-	-
0.06	4.52	3.16162(8)	2.96280(14)	4.7469(3)	-	-
0.1	4.67	3.14036(10)	2.96392(19)	4.7487(5)	-	-
0.2	5.04	3.10136(10)	-	-	-	-
0.3	5.41	3.07307(8)	-	-	4.93242(12)	8.0163(3)

Table 2. The lattice parameters obtained from the Rietveld refinements of the SR-PXD patterns for $(Ti_{0.7}V_{0.3})_{1-z}Fe_zH_x$. The valence-electron concentrations *VEC* of the nominal compositions are also shown.

z	*VEC* [∅]	a_{fcc} [Å]	a_{bcc} [Å]	a_{Laves} [Å]	c_{Laves} [Å]
0	4.30	4.39387(18)	-	-	-
0.03	4.41	4.3903(2)	-	-	-
0.06	4.52	4.3904(4)	-	-	-
0.1	4.67	4.3918(4)	3.220(3)	-	-
0.2	5.04	-	3.1889(6)	-	-
0.3	5.41	-	3.2145(2)	4.9962(2)	8.1543(7)

2.2. In Situ SR-PXD Analysis

Figure 3 presents an *in situ* SR-PXD measurement conducted during heating of $(Ti_{0.7}V_{0.3})_{0.97}Fe_{0.03}H_x$ from room temperature (*RT*) to 500 °C. At $t = 0$ min only diffraction peaks from the fcc hydride phase (γ) are visible. It can be seen that the structure changes when $t = 65$ min and the sample temperature has reached 432 °C. The diffraction peaks are now indexed according to a bcc hydride phase (β) and a primitive tetragonal (pt, $P42/n$) hydride phase (ϵ). The lattice parameters of the latter phase is very close to those reported for TiH ($a = 4.21(4)$ Å and $c = 4.60(2)$ Å [20]). It seems likely that this phase is the hydride of the hcp phase and that it would have transformed back into the hcp alloy (δ) if the temperature was raised higher. At the same time, the lattice parameter reported for fcc TiH_2 ($a = 4.431$ Å [21]) is very close to the value found for $(Ti_{0.7}V_{0.3})_{0.97}Fe_{0.03}H_x$ in Table 2. It is therefore possible that diffraction peaks belonging to this phase is hidden under the ones for the main γ-fcc hydride at $t = 0$ min. It is likely that the hydrogenation behaviour of hcp phase is similar to that of Ti. Thus, we propose that the desorption process follows

$$\gamma(\text{fcc}) \longrightarrow \beta(\text{bcc}) \longrightarrow \alpha(\text{bcc}) \quad (1)$$

$$\zeta(\text{fcc}) \longrightarrow \epsilon(\text{pt}) \longrightarrow \delta(\text{hcp}), \quad (2)$$

where γ is the fcc hydride phase, β is the bcc hydride, α is the main bcc alloy, ζ is a TiH_2-like fcc hydride and ϵ is a TiH-like pt hydride that formed from the δ-hcp impurity phase. Indeed, it is possible that the δ-hcp impurity phase is α-Ti. In that case the hydrogen desorption process is known to involve additional steps than what is suggested in Equation (2) [22], but this is not observed in the present data.

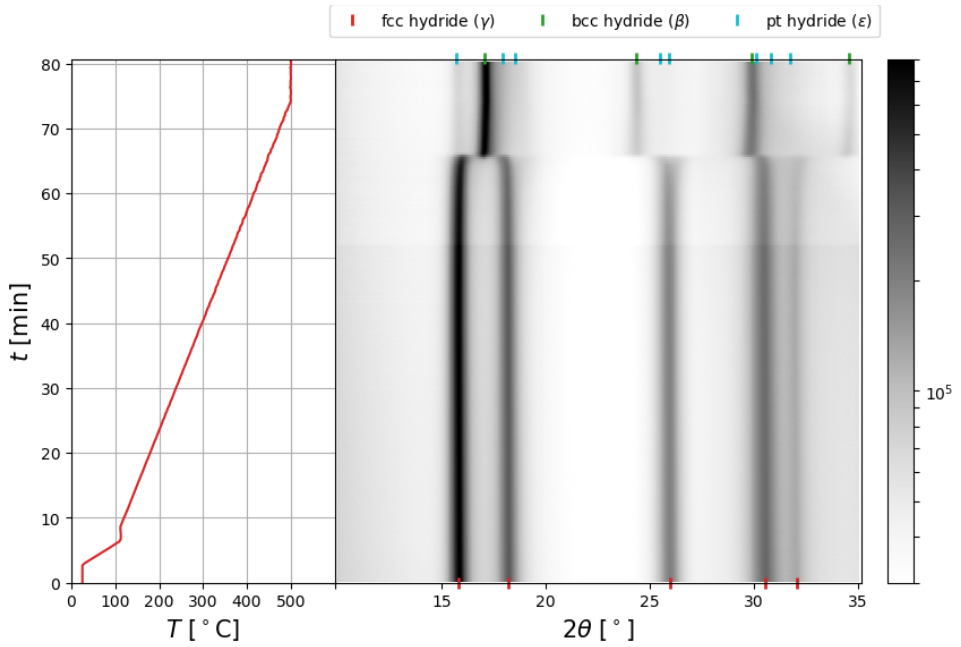

Figure 3. In situ SR-PXD measured during desorption of hydrogen by $(Ti_{0.7}V_{0.3})_{0.97}Fe_{0.03}$. The greyscale shows the logarithmic intensity, and the temperature T at the sample position is indicated as a function of time t. The heating rate was 20 °C/min in the first and 5 °C/min in the second linear heating region. Peaks belonging to known phases are indexed by colored ticks. $\lambda = 0.6973$ Å.

2.3. Thermal Analysis and Sieverts Measurements

Figure 4a presents the extent of reactions $\xi(t)$ for the first two hydrogen absorption cycles for the considered compounds. $\xi(t)$ is a dimensionless parameter that measure the progression of the absorption-reaction. For the system $(Ti_{0.7}V_{0.3})_{1-z}Fe_zH_x$ it is defined as $\xi(t) = x(t)/x(t_{final})$ where $x(t)$ and $x(t_{final})$ are the stoichiometric coefficient of hydrogen in the hydride at time t and when the reaction is complete, respectively. The samples were activated by heating to 500 °C under dynamic vacuum for at least 8 h before they were cooled to *RT* and exposed to 19.9(3) bar H_2 at time $t = 0$. The hydrogen was removed from the samples between the two measurements by re-exposing them to dynamic vacuum at 500 °C for at least 8 h. Figure 4a shows that the hydrogen absorption kinetics of the Fe-free system is very fast and for all practical purposes complete within a few minutes. The introduction of Fe enhances the absorption kinetics further which is opposite to what was reported by Kagawa et al. for the V-rich part of the Ti−V−Fe system [14]. One should note that during the initial step of the measurements the calculated $\xi(t)$ is irreliable and can reach unphysical values larger than one. This is attributed to rapid, local temperature increase due to the exothermal reaction which is difficult to correct for in the calculations. The hydrogen absorption kinetics improve significantly from the first to the second cycle, while there is no significant change between the second and third cycle (not shown). Thus, the improvement seems to be related to the increase in reactive particle surface due to the disintegration of the bulk particles under interaction with hydrogen during the first absorption [23]. It is unclear whether the Ti_4Fe_2O oxide phase influence the hydrogen sorption process. However, it seems clear that it does not cover and passivate the surface since the samples with the highest amount of oxide also have the fastest hydrogen sorption kinetics. Therefore, it seems likely that the oxide is present as separate particles rather than a thin surface layer on the alloy. This is supported by the sharp Bragg peaks from the oxide. Moreover, the Ti_4Fe_2O particles may catalyze hydrogen sorption.

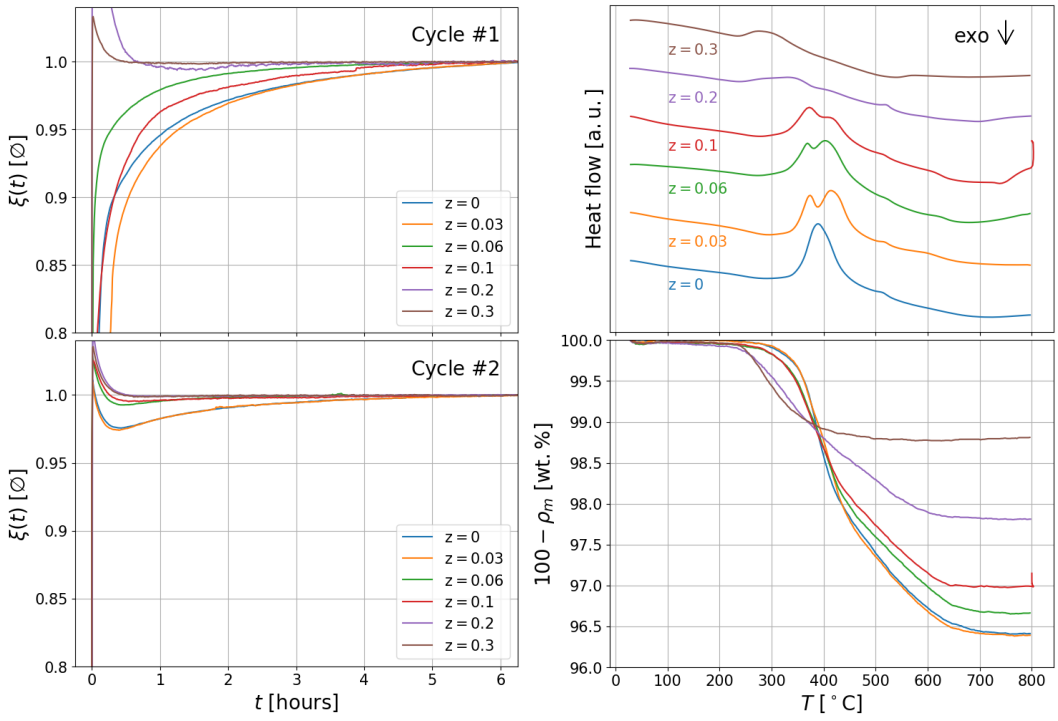

(**a**) (**b**)

Figure 4. (**a**) The extent of reaction $\xi(t)$ for the first two hydrogen absorption cycles by as-cast $(Ti_{0.7}V_{0.3})_{1-z}Fe_z$ when exposed to an initial hydrogen pressure of 19.9(3) bar H_2. (**b**) thermogravimetric differential scanning calorimetry (TG/DSC) measurements of $(Ti_{0.7}V_{0.3})_{1-z}Fe_zH_x$ measured at 10 °C/min. The upper and lower panels presents the DSC and TGA measurements, respectively.

Figure 4b shows the combined thermogravimetric analysis and differential scanning calorimetry (TG/DSC) measurements during hydrogen desorption from the $(Ti_{0.7}V_{0.3})_{1-z}Fe_zH_x$ hydrides. The DSC heat flow signals shows that the onset temperature at which the desorption is initiated is shifted towards lower temperatures when the amount of Fe increases. The desorption enthalpy per mole H_2 was determined by integrating the measured heat flow signals using the Netzsch PROTEUS evaluation software. For $Ti_{0.7}V_{0.3}$ the obtained value is $\Delta H_{z=0} = 74 \pm 6$ kJ/mol H_2. For the other samples, ΔH_z decreases linearly in accordance with the relation

$$\Delta H_z / \Delta H_{z=0} = 1.0 - 0.8 \cdot z. \quad (3)$$

Thus, the Fe destabilize the hydrides. Figure 5 presents the hydrogen contents that were obtained from the TG and the manometric measurements. The error bars for the gravimetric values show the standard deviations calculated from ten independent TG measurements of each sample, while the error bars of the manometric points are calculated from the uncertainties in the pressure sensors and in the calibrated volumes. The manometric measurements were performed with two different initial hydrogen pressures, 19.9(3) and 100(2) bar. It can be seen that a higher hydrogen content is obtained when the pressure is increased and reaches the stoichiometric value $[H]/[M] = 2$ for the Fe-free sample. Furthermore, the maximum hydrogen content decreases with increasing Fe-content. This is in agreement with the reported observation that Fe form hydrogen-free clusters within the alloy [15]. The gravimetric and manometric values are in agreement for $z \leq 0.1$ when the initial pressure is limited to 20 bar H_2. Moreover, at this pressure the hydrogen capacity is not influenced significantly by the addition of Fe and reach 3.2(3) wt% for $z = 0.1$. However, for higher Fe-contents the capacity is reduced and the gravimetric and manometric estimates differ. This observation suggests that some hydrogen was outgassed from the less stable hydrides when they were retrieved from the hydrogen atmosphere inside the Sieverts apparatus.

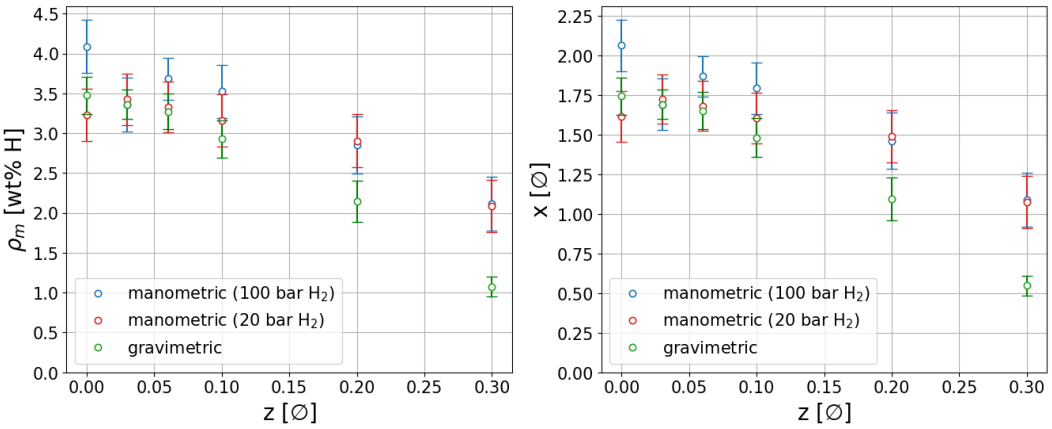

Figure 5. The hydrogen content in $(Ti_{0.7}V_{0.3})_{1-z}Fe_zH_x$ measured gravimetrically by TG and manometrically in the Sieverts apparatus at two different initial hydrogen pressures, 19.9(3) bar and 100(2) bar respectively.

Figure 6 shows the DSC heat flow signals and the corresponding Kissinger analyses of the two systems $Ti_{0.7}V_{0.3}$ and $(Ti_{0.7}V_{0.3})_{0.9}Fe_{0.1}$. For the Fe-free sample it seems to be two major events in the desorption process, as indicated by the two peaks that are marked 1 and 2 in the heat flow signals of Figure 6a. Peak 2 occurs at a significantly higher temperature than peak 1, which is the main part of the desorption. When Fe is introduced into the alloy the main event splits into two which are marked by 1*a* and 1*b* in Figure 6b, respectively. Such splitting is observed for all the Fe containing hydrides regardless of the amount of Fe present in the alloy. The activation energies for the three events were estimated by Kissingers method and are shown in Figure 7. There are some clearly visible trends. The activation energy of the main event $E_{A,1b}$ tends to decrease with increasing z. This behaviour is similar to what was observed by Suwarno et al. for the Ti-rich Ti–V–Cr system under addition of Cr to the alloy [24]. A similar trend is observed for event 1*a* with activation energy $E_{A,1a}$. The activation energy of the high-temperature event $E_{A,2}$ finally seems to assume a rather constant value regardless of z. This indicates that the third event is associated with hydrogen desorption from the Fe-free interstitial sites in the metal hydride. With respect to the discussion in Section 2.2, it is likely that this event is related to hydrogen desorption from ϵ-pt hydrides since it occurs at a higher temperature than the maximum in the in situ measurement. Interestingly, the activation energies reported for TiH_2 is compareable with the values obtained for $E_{A,2}$ [22]. Moreover, the desorption peaks of TiH_2 are within the same temperature range as observed for the high-temperature events in Figure 6. Thus, we conclude that there is strong evidence that the hcp impurity phase is α-Ti.

This work was motivated by the possibility to replace expensive V by the much cheaper ferrovanadium in Ti−V-based bcc alloys for hydrogen storage. It is clear that the hydrogen sorption properties of the system $(Ti_{0.7}V_{0.3})_{1-z}Fe_z$ is improved in many aspects with the addition of Fe when $z \leq 0.1$. Within this range, the main phase of the alloys is bcc ($Im\bar{3}m$) and fcc hydrides are formed from these in a gas-solid state reaction. The absorption kinetics of the reactions are fast, and they are completed within minutes when the samples are exposed to modest hydrogen pressures ∼20 bar at *RT*. Manometric and gravimetric measurements of the hydrogen contents indicate that the hydrogen storage capacity is ∼3.5 wt%. The influence of Fe addition is within the error bars if $z \leq 0.1$ and the initial hydrogen pressure is limited to 20 bar. For higher Fe-contents the capacity is reduced. In general, increasing the Fe-content lowers the enthalpy, onset temperature and activation energy for the hydrogen desorption.

As a complete substitution of V by ferrovanadium in the reference system $Ti_{0.7}V_{0.3}$ corresponds to $z \approx 0.07$ we might conclude this work by stating that such a substitution seems to be advantageous, not only from an economical point of view, but also based on the material properties. It should however be stated that ferrovanadium contains other impurities, such as Si and Al. It is recommended that

further studies investigate the influence of these elements upon the crystalline structure and hydrogen sorption properties of Ti-rich Ti−V−Fe alloys. The long-term cyclability of the material should also be investigated in further detail. Pressure-composition isotherms should also be measured to distinguish between kinetic and thermodynamic effects. Finally, since the samples containing Ti_4Fe_2O show the fastest hydrogen absorption, it could be interesting to investigate the catalytic activity of this phase for hydrogen sorption processes in general.

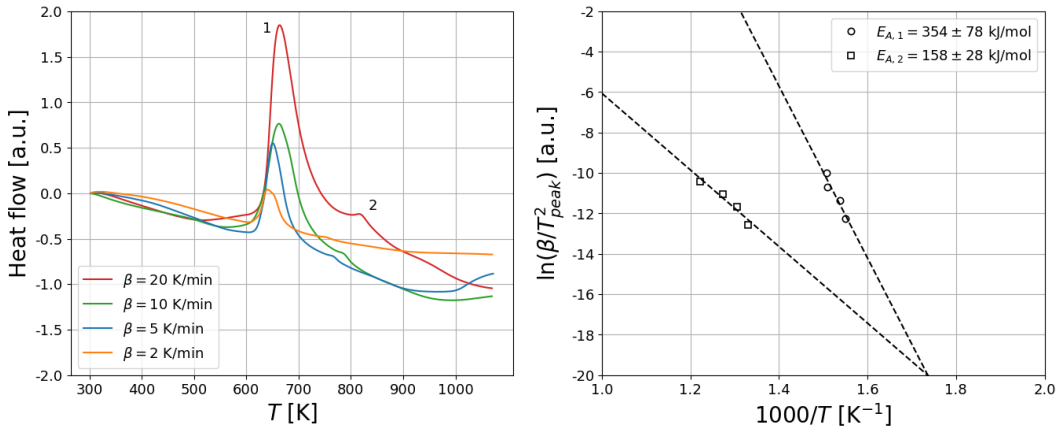

(**a**)

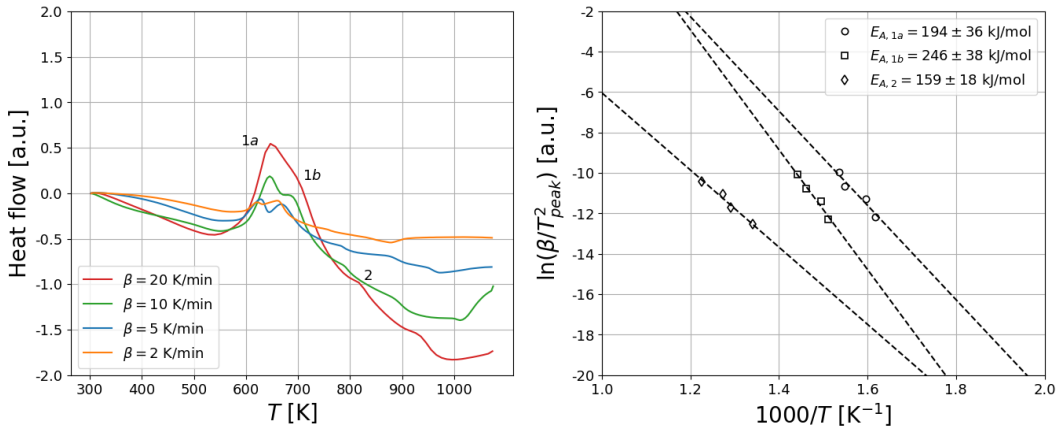

(**b**)

Figure 6. Kissinger analyses of DSC measurements during desorption of hydrogen from $Ti_{0.7}V_{0.3}H_x$ (**a**) and $(Ti_{0.7}V_{0.3})_{0.9}Fe_{0.1}H_x$ (**b**) at different heating rates β.

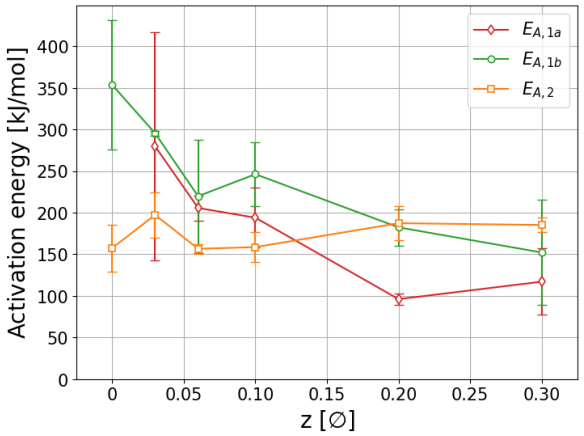

Figure 7. Activation energies E_A for three different events determined by the Kissinger method applied on DSC measurements during hydrogen desorption from $(Ti_{0.7}V_{0.3})_{1-z}Fe_zH_x$ at different heating rates.

3. Materials and Methods

3.1. Synthesis

Six samples of $(Ti_{0.7}V_{0.3})_{1-z}Fe_z$ with $z \in \{0, 0.03, 0.06, 0.1, 0.2, 0.3\}$ were synthesised from −200 mesh powders of Ti and Fe (Alfa Aesar, 99.5% purity; metal basis) and V cut from a 0.5 mm thick sheet (Aldrich Chemistry, 99.7% purity; metal basis) by arc melting under Ar atmosphere. A piece of Ti was first melted to serve as an oxygen getter. The samples were then melted five times to enhance homogeneity and the cast buttons were turned around between each melting. The mass losses during arc melting were at most 1.3 wt%, and thus the final compositions are very close to the nominal ones. Activation was performed by exposing the as-cast materials to two consecutive cycles of dynamic vacuum and 19.9(3) bar H_2 at 350 °C inside a Sieverts apparatus that is described elsewhere [25]. The samples were then cooled to *RT* and hydrogenated at the same pressure. Parts of the resultant hydride powders were retrieved from the Sieverts apparatus for analysis while the rest was exposed to dynamic vacuum and 500 °C for desorption to obtain the powdered hydrogen-free alloys. All hydrides and powdered alloys were handled and storaged inside an MBraun Unilab glove box with purified Ar atmosphere (<1 ppm O_2 and H_2O).

3.2. SR-PXD Experiments

Both ex situ and in situ SR-PXD data were collected at the Swiss-Norwegian Beamline BM01A at the European Synchrotron Radiation Facility (ESRF) in Grenoble, France. The diffraction patterns were recorded by a Dectris Pilatus 2M pixel area detector [26] positioned 246.38 mm from the sample. The wavelength was $\lambda = 0.6973$ Å. The samples were contained in 0.5 mm inner diameter borosilicate glass capillaries that were sealed in Ar atmosphere during the ex situ experiments. In the in situ experiment the sample was contained inside a sapphire capillary connected to an in-house built gas rig. The sample was first heated to 100 °C at 20 °C/min. The heating rate was then reduced to 5 °C/min and the sample heated to a final temperature of 500 °C. The sample was under dynamic vacuum during the entire process. Phase identification was performed by search-matchings with the PDF-4 database and the structures were subsequently refined using the General Structure Analysis System (GSAS) [27,28]. In these refinements, the background was fitted by a 16th order shifted Chebyschev polynomial. Five peak shape parameters were refined alongside the displacement factors and lattice parameters.

3.3. Thermal Analysis

Thermal analysis was performed with a Netzsch STA 449 F3 Jupiter apparatus which performs TG and DSC simultaneously. ∼20 mg of the respective samples were placed inside alumina crucibles equipped with pierced lids. The samples were briefly exposed to air when transferred to the apparatus where they were protected by flowing Ar (50 mL/min) during the measurements. Overlapping peaks associated with different events in the DSC heat flow signals were in certain measurements deconvoluted using Gaussian functions in the Fityk software [29] to determine the peak positions used in the Kissinger analyses.

3.4. Sieverts Measurements

Kinetic measurements of hydrogen absorption were measured manometrically with an in-house built Sieverts apparatus [25]. During these measurements the samples were contained in a stainless steel autoclave. Two series of experiments were performed. In the first of these the samples were exposed to 19.9(3) bar H_2 at *RT*. The second measurement series was also conducted at *RT* but with a higher hydrogen pressure of 100(2) bar.

Supplementary Materials: The following are available online at www.mdpi.com/xxx/s1, Figure S1. Rietveld refinements of SR-PXD patterns of $(Ti_{0.7}V_{0.3})_{0.97}Fe_{0.03}$, $(Ti_{0.7}V_{0.3})_{0.94}Fe_{0.06}$ and their associated hydrides.

Author Contributions: Conceptualization, M.H.S. and B.C.H.; investigation and analysis, M.M.N.; writing—original draft preparation, M.M.N.; writing—review and editing, M.H.S.; A.A.G. and B.C.H. All authors have read and agreed to the published version of the manuscript.

Funding: M.M.N. acknowledge funding through the Functional Hydrides (FunHy) project with grant number 81942 of the NordForsk Nordic Neutron Science Programme.

Acknowledgments: The authors wish to thank the staff at the Swiss-Norwegian beamline (BM01A) at the European Synchrotron Radiation Facility (ESRF) in Grenoble, France for skillful assistance during the SR-PXD experiments.

Conflicts of Interest: The authors declare no conflict of interest.

References

1. Mohtadi, R.; Orimo, S.-I. The renaissance of hydrides as energy materials. *Nat. Rev. Mater* **2016**, *2*, 1–15. [CrossRef]
2. Hirscher, M.; Yartys, V.A.; Baricco, M.; Bellosta von Colbe, J.M.; Blanchard, D.; Bowman, R.C.; Broom, D.P.; Buckley, C.E.; Chang, F.; Chen, P.; et al. Materials for hydrogen-based energy storage—Past, recent progress and future outlook. *J. Alloys Compd.* **2020**, *827*, 153548. [CrossRef]
3. Milanese, C.; Jensen, T.R.; Hauback, B.C.; Pistidda, C.; Dornheim, M.; Yang, H.; Lombardo, L.; Züttel, A.; Filinchuk, Y.; Ngene, P.; et al. Complex hydrides for energy storage. *Int. J. Hydrog. Energy* **2019**, *44*, 7860–7874. [CrossRef]
4. Yartys, V.A.; Lototskyy, M.V.; Akiba, E.; Albert, R.; Antonov, V.E.; Ares, J.R.; Baricco, M.; Bourgeois, N.; Buckley, C.E.; Bellosta von Colbe, J.M.; et al. Magnesium based materials for hydrogen based energy storage: Past, present and future. *Int. J. Hydrog. Energy* **2019**, *44*, 7809–7859. [CrossRef]
5. Maeland, A.J.; Gibb, T.R.P.; Schumacher, D.P. A novel hydride of vanadium. *J. Am. Chem. Soc.* **1961**, *83*, 3728–3729. [CrossRef]
6. Maeland, A.J. Investigation of the vanadium-hydrogen system by X-ray diffraction techniques. *J. Am. Chem. Soc.* **1961**, *68*, 2197–2200.
7. Nagel, H.; Perkins, R.S. Crystallographic investigation of ternary titanium vanadium hydrides. *Z. Für Met.* **1961**, *66*, 362–366.
8. Hagi, T.; Sato, Y.; Yasuda, M.; Tanaka, K. Structure and phase diagram of Ti−V−H system at room temperature. *Trans. Jpn. Inst. Met.* **1987**, *28*, 198–204. [CrossRef]
9. Kagawa, A. Absorption of hydrogen by vanadium-titanium alloys. *Rep. Fac. Eng. Nagasaki Univ.* **1995**, *25*, 233–239.
10. Kumar, S.; Jain, A.; Ichikawa, T.; Kojima, Y.; Dey, G.K. Development of vanadium based hydrogen storage material: A review. *Renew. Sustain. Energy Rev.* **2017**, *72*, 791–800. [CrossRef]
11. Maeland, A.J.; Libowitz, G.G.; Lynch, J.F.; Rak, G. Hydride formation rates of bcc group V metals. *J. Less Common Met.* **1984**, *104*, 133–139. [CrossRef]
12. Maeland, A.J.; Libowitz, G.G.; Lynch, J.P. Hydride formation rates of titanium-based bcc solid solution alloys. *J. Less Common Met.* **1984**, *104*, 361–364. [CrossRef]
13. Lynch, J.F.; Maeland, A.J.; Libowitz, G.G. Lattice parameter variation and thermodynamics of dihydride formation in the vanadium-rich V−Ti−Fe/H_2 system. *Z. Für Phys. Chem.* **1985**, *145*, 51–59. [CrossRef]
14. Kagawa, A.; Ono, E.; Kusakabe, T.; Sakamoto, Y. Absorption of hydrogen by vanadium-rich V−Ti-based alloys. *J. Less Common Met.* **1991**, *172*, 64–70. [CrossRef]
15. Mauroy, H.; Klyukib, K.; Shelyapina, M.G.; Thøgersen, A.; Keen, D.; Hauback, B.C.; Sørby, M.H. Short-range structure of $Ti_{0.63}V_{0.27}Fe_{0.10}D_{1.73}$ from neutron total scattering and Reverse Monte Carlo modelling. *Energies* **2020**, *13*, 1947. [CrossRef]
16. Wood, R.M. The lattice constants of high purity alpha titanium. *Proc. Phys. Soc.* **1962**, *80*, 783. [CrossRef]
17. Makinson, J.D.; Lee, J.S.; Magner, S.H.; De Angelis, R.J.; Weins, W.N.; Hieronymus, A.S. X-ray diffraction signatures of defects in nanocrystalline materials. *Adv. X-ray Anal.* **2000**, *42*, 407–411.
18. Balogh, L.; Ribárik, G.; Ungár, T. Stacking faults and twin boundaries in fcc crystals determined by X-ray diffraction profile analysis. *J. Appl. Phys.* **2006**, *100*, 023512. [CrossRef]
19. Matsuda, J.; Akiba, E. Lattice defects in V−Ti bcc alloys before and after hydrogenation. *J. Alloys Compd.* **2013**, *581*, 369–372. [CrossRef]
20. Numakura, H.; Koiwa, M. Hydride precipitation in titanium. *Acta Metall.* **1984**, *32*, 1799–1807. [CrossRef]

21. Irving, P.E.; Beevers, C.A. Some metallographic and lattice parameter observations on titanium hydride. *Metall. Trans.* **1971**, *2*, 613–615. [CrossRef]
22. Ma, M:; Liang, L.; Wang, L.; Wang, Y.; Cheng, Y.; Tang, B.; Xiang, W.; Tan, X. Phase transformations of titanium hydride in thermal desorption process with different heating rates. *Int. J. Hydrog. Energy* **2015**, *40*, 8926–8934. [CrossRef]
23. Liu, Z.; Xiong, L.; Liu, S. Effect of surface morphology on initial hydrogen diffusion in vanadium alloys. *Mater. Lett.* **2019**, *241*, 100–103. [CrossRef]
24. Suwarno, S.; Solberg, J.K.; Maehlen, J.P.; Krogh, B.; Yartys, V.A. Influence of Cr on the hydrogen storage properties of Ti-rich Ti−V−Cr alloys. *Int. J. Hydrog. Energy* **2012**, *37*, 7624–7628. [CrossRef]
25. Brinks, H.W.; Fossdal, A; Bowman, R.C.; Hauback, B.C. Pressure-composition isotherms of $TbNiAlH_x$. *J. Alloys Compd.* **2006**, *417*, 92–95. [CrossRef]
26. Dyadkin, V.; Pattison, P.; Dmitriev, V.; Chernyshov, D. A new multipurpose diffractometer PILATUS @ SNBL. *J. Synchrotron Radiat.* **2016**, *23*, 825–829. [CrossRef] [PubMed]
27. Larson, A.C.; Von Dreele, R.B. *General Structure Analysis System (GSAS)*; Los Alamos National Laboratory: Santa Fe, NM, USA, 1994; pp. 86–748.
28. Toby, B.H. EXPGUI, a graphical user interface for GSAS. *J. Appl. Crystallogr.* **2001**, *34*, 210–213. [CrossRef]
29. Wojdyr, M. Fityk: A general—Purpose peak fitting program. *J. Appl. Crystallogr.* **2010**, *43*, 1126–1128. [CrossRef]



© 2020 by the authors. Licensee MDPI, Basel, Switzerland. This article is an open access article distributed under the terms and conditions of the Creative Commons Attribution (CC BY) license (http://creativecommons.org/licenses/by/4.0/).